Supporting information

Simultaneous removal of C_2H_2 and C_2H_6 for C_2H_4 purification by robust MOFs featuring high density of heteroatoms

Shikai Xian,[a,b] Junjie Peng,[c] Haardik Pandey,[d] Wells Graham,[d] Liang Yu,[c] Hao Wang,[a] Kui Tan,[e] Timo Thonhauser[d] and Jing Li[b,a,*]

a. Hoffmann Institute of Advanced Materials, Shenzhen Polytechnic, 7098 Liuxian Boulevard., Shenzhen, Guangdong 518055, China
b. Department of Chemistry and Chemical Biology, Rutgers University, 123 Bevier Road, Piscataway, New Jersey 08854, USA
c. School of Environmental and Chemical Engineering, Foshan University, 18 Jiangwan 1st Road, Chancheng, Foshan 528000, China
d. Department of Physics and Center for Functional Materials, Wake Forest University, 1834 Wake Forest Road, Winston-Salem, North Carolina 27109, USA
e. Department of Chemistry, University of North Texas, Denton, Texas 76201, USA

Content

S1. Synthesis and general methods

1.1 Reagents and solvents

   All reagents were purchased commercially and used as received. Aluminum chloride hexahydrate was purchased from Alfa Aesar; 3,5-pyrazoledicarboxylic acid monohydrate, 2,5-furandicarboxylic acid, and 2,5-thiophenedicarboxylic acid were all supplied by TCI America; Sodium hydroxide was purchased from Acros Organics; The high-purity gases used in adsorption experiments were obtained from Praxair Inc. (New Jersey)

1.2 Preparation of MOF-303, MIL-160, and CAU-23

   MOF-303 was prepared by using the procedure reported by Yaghi et al.[1] with modification. 1.04 g Aluminum chloride hexahydrate ($AlCl_3 \cdot 6H_2O$, 4.308 mmol) and 0.75 g 3,5-pyrazoledicarboxylic acid monohydrate (H_3PDC, 4.308 mmol) were dissolved in 72 mL water in a 200 mL glass flask, 3 mL aqueous NaOH (0.26 g, 6.5 mmol) were added dropwise to the above mixture under stirring. The flask was then heated at 100 ºC with reflux for 12h. After cooling down to room temperature, the as-synthesized MOF-303 powder was obtained by filtration. To remove the remaining 3,5-pyrazoledicarboxylic acid, the powder was washed thoroughly with water, followed by heated under vacuum at 150 ºC for 12h. MIL-160 and CAU-23 were obtained through the same process as that of MOF-303 by replacing the ligand 3,5-pyrazoledicarboxylic acid monohydrate with 2,5-furandicarboxylic acid and 2,5-thiophenedicarboxylic acid, respectively.

1.3. Instrument and Characterization

   Powder X-ray diffraction (PXRD) patterns were collected on an Ultima IV X-ray diffractometer between a scanning range of 3°-35° at 2.0 deg/min. Thermogravimetric analysis (TGA) was performed on a TA Q5000-IR analyzer, with temperature increased at a ramping rate of 10 K/min from ambient temperature to

973 K under a flowing nitrogen environment. Nitrogen adsorption isotherms were obtained at 77 K using a Micromeritics 3Flex analyzer. The BET model was chosen to evaluate the specific surface area, while the HK (Horvath-Kawazoe) method was applied to acquire the micropore size distribution.

1.4 Hydrocarbon adsorption experiments

C_2H_6, C_2H_4, and C_2H_2 sorption isotherms were performed on the Micromeritics 3Flex analyzer. Volumetric sorption data were measured at various temperatures and pressures up to 1 bar. The desired temperature (298 K-323 K) was controlled through employing water bath circulated by a precise temperature thermostat. Prior to data collection, 80–100 mg samples were degassed at 423 K for 12 h.
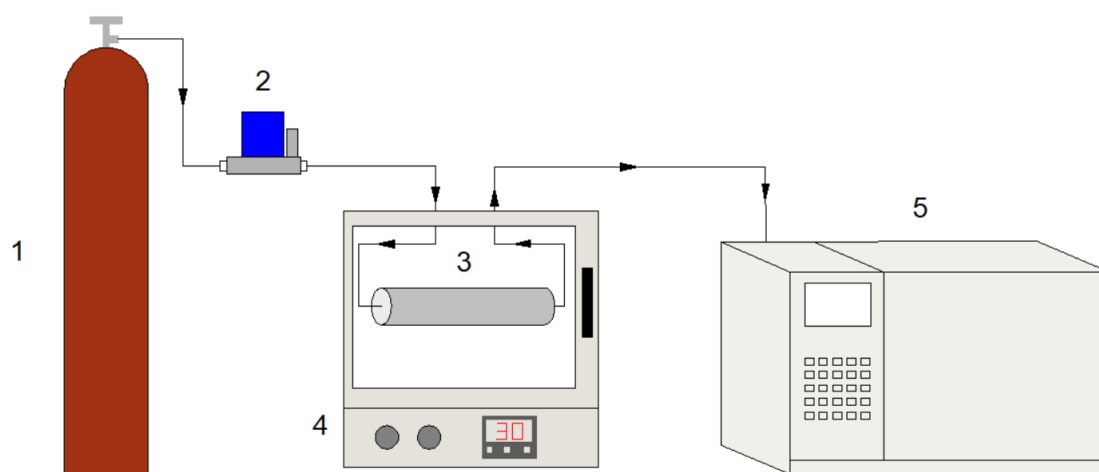
1.5 Breakthrough experiments

Fig. S1. Schematic illustration of the home-made breakthrough assembly. (1. Gas mixture source; 2. Mass flowmeter; 3. Adsorption column; 4. Temperature-controlled oven; 5. Agilent gas chromatograph system).

Breakthrough curves were obtained on an self-assembled experimental setup (Fig. S1). Under the control of a mass flow meter, the velocity was set to be 1 mL/min for the binary mixture C_2H_6/C_2H_4 (1:15, v/v) and ternary mixture $C_2H_6/C_2H_4/C_2H_2$ (1:1:1, v/v). A small-scale adsorption column was made by packing about 0.2 g of an activated sample into a long stainless hollow cylinder. The real time concentration of the effluent component was probed by a gas chromatography (GC)

spectrometer (Agilent, 7890A). Before the experiment, the packed column was heated at 423 K under 5 mL/min He flow for 1h. After the breakthrough experiment, the desorption curves were measured at 298 K or 323 K under 5 mL/min He flow.

1.6 Theoretical calculation method

All *ab initio* calculations were performed using density functional theory (DFT) in VASP (Vienna Ab Initio Simulation Package)[2, 3], with vdW-DF functional[4-6] to take into account important van der Waals interactions. All the MOF unit cells were optimized by carrying out spin-polarized calculations, with SCF convergence of 0.1 meV and the plane wave energy cut-off set at 600 eV. The unit cell parameters and atoms were allowed to move till the force acting between atoms reached below 5 meV/Å. Potential binding sites were studied by placing C_2H_2, C_2H_4, and C_2H_6 molecules in the MOF-303 at various sites and all the atoms were allowed to relax in accordance with the convergence condition. Difference in the total energies of the MOF unit-cell and the guest molecules was used to calculate the corresponding binding energies. Induced charge densities were also calculated that maps the variation in charge density upon introduction of the guest molecules and help identifying the interactions happening at the binding sites.

1.7 Ideal adsorbed solution theory (IAST) selectivity calculations

IAST is a common method to evaluate adsorption selectivities of binary or multinary mixtures from pure-component adsorption isotherms.[7, 8]

$$S = \frac{X_A/X_B}{Y_A/Y_B} \qquad\qquad (S1)$$

Where S is the selectivity of component A relative to B. X_A and X_B are the molar fractions of components A and B in the adsorption phase, respectively. Y_A and Y_B are molar fractions of components A and B in the gas phase, respectively. Dual-site Langmuir-Freundlich (DSLF) equation was used to simulate the isotherms of MOF-303, MIL-160, and CAU-23 shown as follows:[9, 10]

$$q = q1\frac{b1p^{c}}{1+b1p^{c}} + q2\frac{b2p^{t}}{1+b2p^{t}} \qquad (S2)$$

Where p is the equilibrium pressure of the gas phase and adsorbed phase; q_a and q_b are the saturated capacity of site a and b, respectively; b1 and b2 are the affinity coefficients of site a and b, respectively; c and t are for the heterogeneity from an ideal homogeneous surface of site a and b, respectively.

1.8 Isosteric heat calculation

The isosteric heat (Q_{st}) was calculated by equation S4. Before the calculation, the isotherms tested at 303 K and 313 K were fitted by the Virial equation (equation S3). p is the pressure described in Pa, N is the adsorbed amount in mmol/g, T is the temperature in K, a_i and b_j are Virial coefficients, and m and n are the number of coefficients used to describe the isotherms, R is the universal gas constant.

$$\text{Ln}p = \ln N + \left(\frac{1}{T}\right)\sum_{i=0}^{m} a_i \times N^i + \sum_{j=0}^{n} b_j \times N^j \qquad (S3)$$

$$Q_{st} = -R \times \sum_{i=0}^{m} a_i \times N^i \qquad (S4)$$

S2. N₂ isotherms at 77 K and pore size distribution
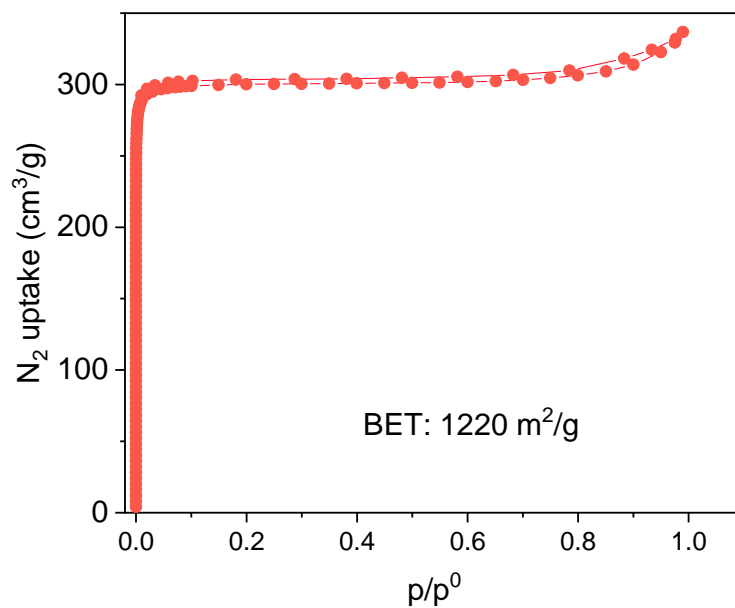

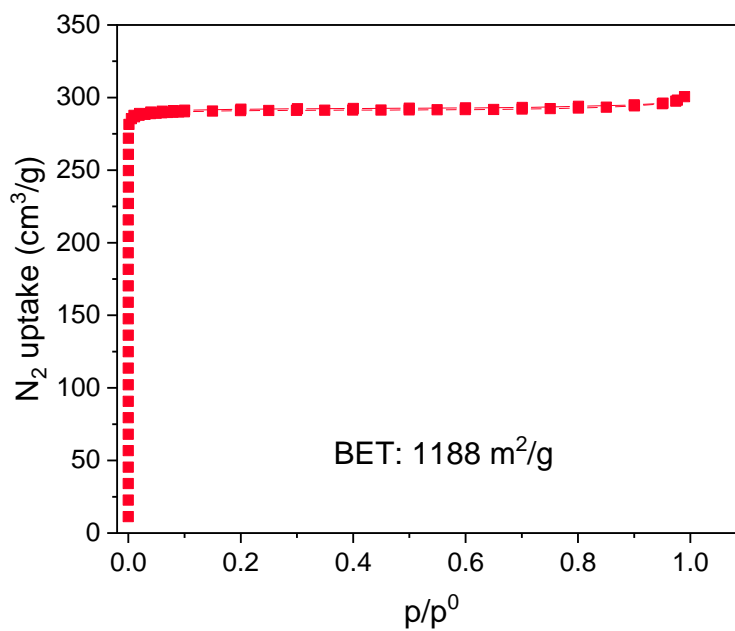Fig. S2. N₂ adsorption-desorption isotherms of MOF-303 at 77 K.

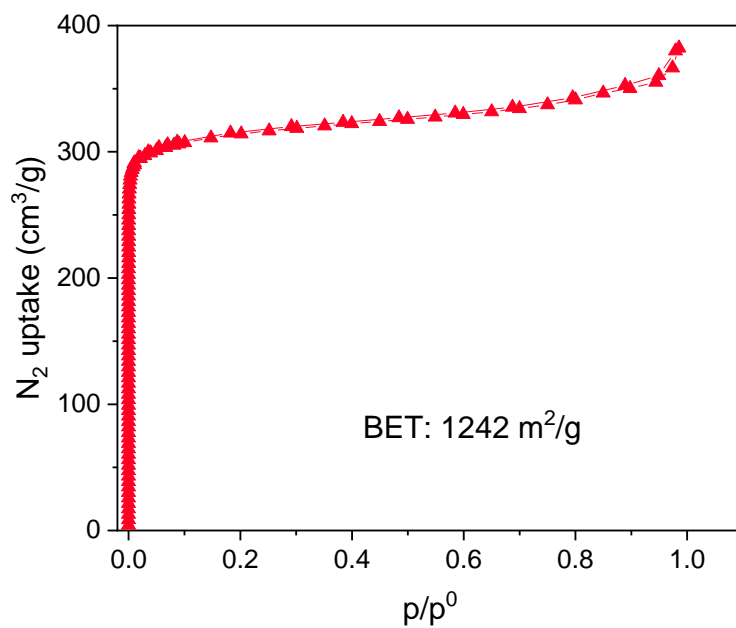Fig. S3. N₂ adsorption-desorption isotherms of MIL-160 at 77 K.

Fig. S4. N_2 adsorption-desorption isotherms of CAU-23 at 77 K.
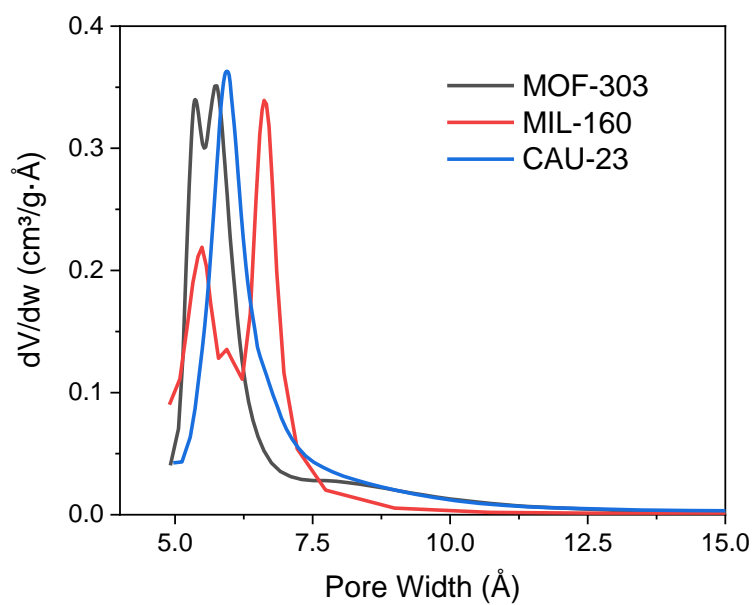

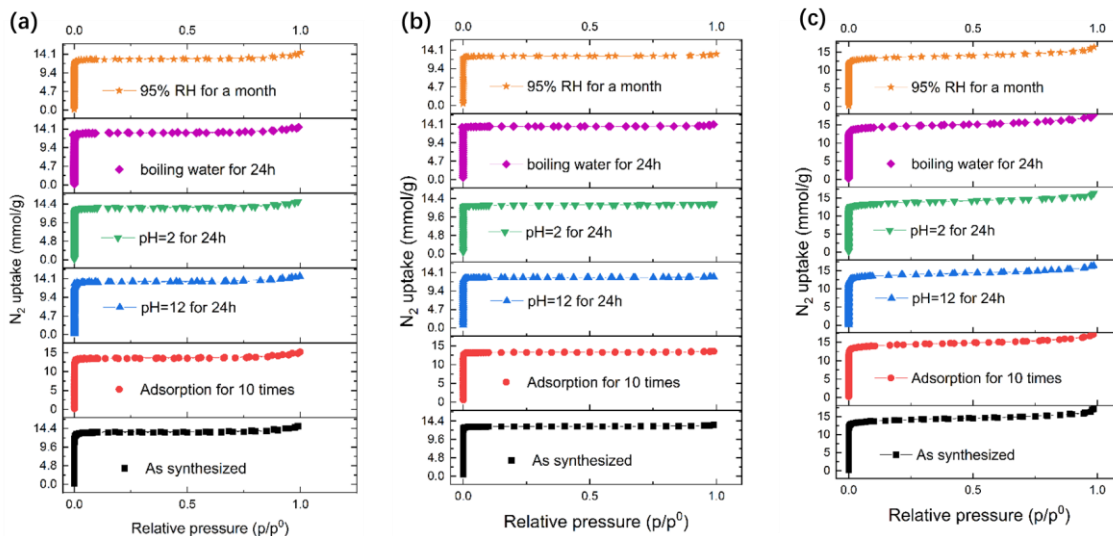Fig. S5. HK pore size distribution of MOF-303, MIL-160, and CAU-23.

Fig. S6. The N$_2$-77 K adsorption isotherms of the (a) MOF-303, (b) MIL-160, and (c) CAU-23 samples after being treated with different conditions.
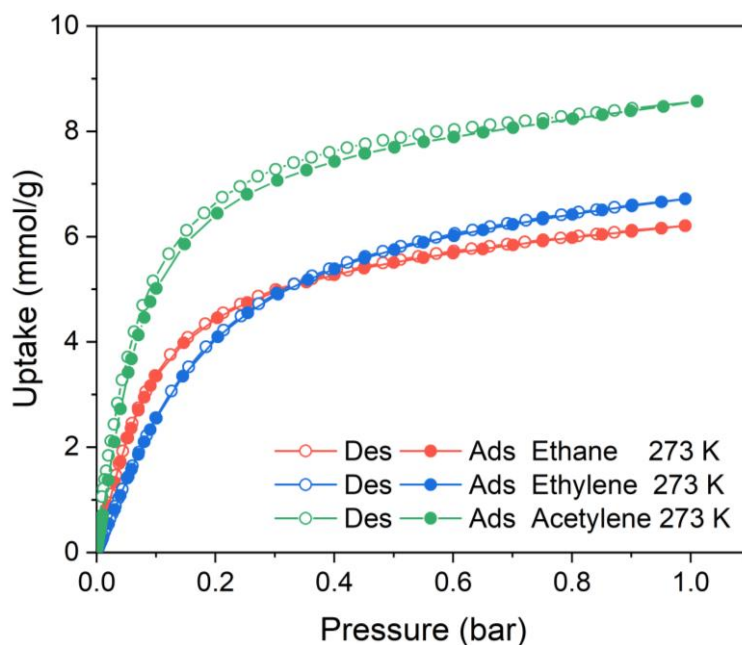
S3. Hydrocarbon isotherms

Fig. S7. Adsorption-desorption isotherms of MOF-303 for C$_2$H$_2$, C$_2$H$_4$, and C$_2$H$_6$ at 273 K.
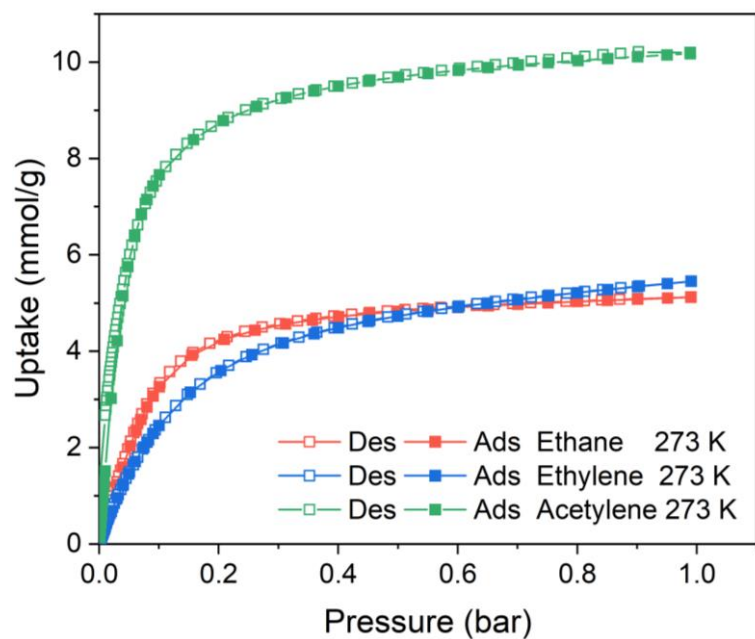
Fig. S8. Adsorption-desorption isotherms of MIL-160 for C_2H_2, C_2H_4, and C_2H_6 at 273 K.
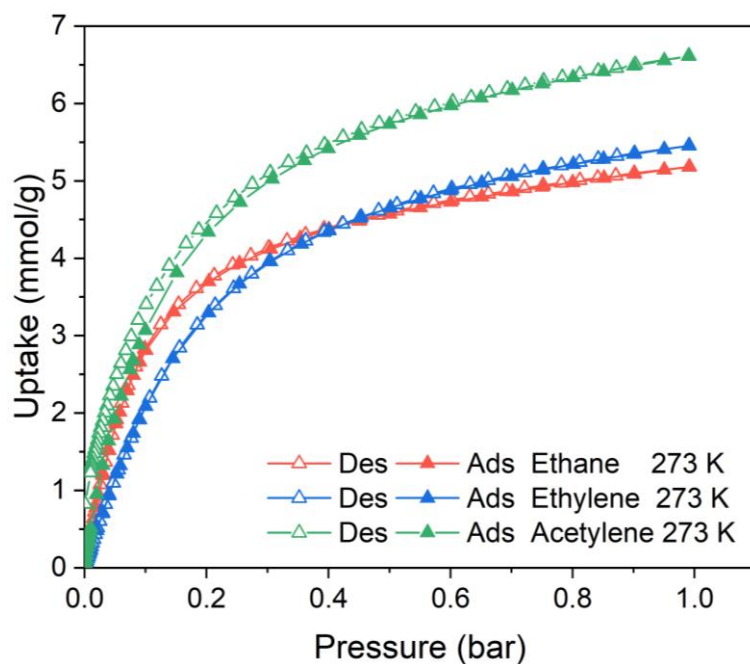

Fig. S9. Adsorption-desorption isotherms of CAU-23 for C_2H_2, C_2H_4, and C_2H_6 at 273 K.
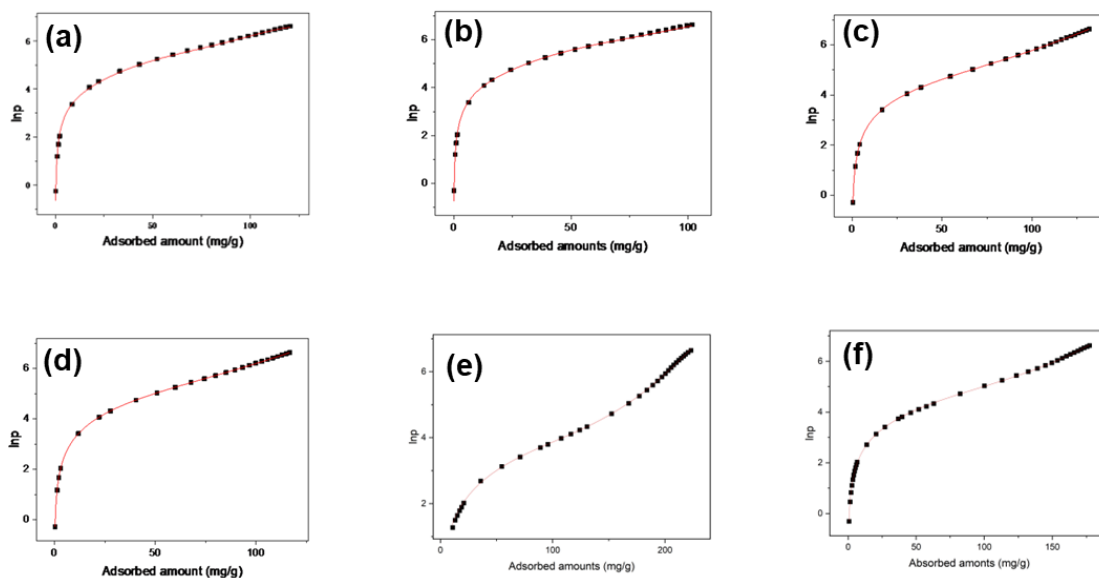
S4. Isosteric heat fitting

Fig. S10. Virial fitting of MOF-303 for (a)C_2H_4 at 303 K, (b) C_2H_4 at 313 K, (c) C_2H_6 at 303 K, (d) C_2H_6 at 313 K, (e) C_2H_2 at 273 K, and (d) C_2H_2 at 298 K.

Table S1. Virial fitting parameters of MOF-303 for C_2H_4, C_2H_6, and C_2H_2.

parameters	C_2H_4	C_2H_6	C_2H_2
a0	-2692.01196	-3021.41191	-3573.76303
a1	-36.12928	-15.54279	3.04109
a2	0.61735	0.06661	-0.02664
a3	6.11461E-5	3.3074E-6	2.21783E-6
a4	-1.877E-7	-1.08077E-8	-3.79295E-9
b0	10.30939	10.57015	12.09398
b1	0.08794	0.05096	-0.01215
b2	-6.93943E-4	-1.4776E-4	2.03216E-4
R^2	0.99764	0.99999	0.99992
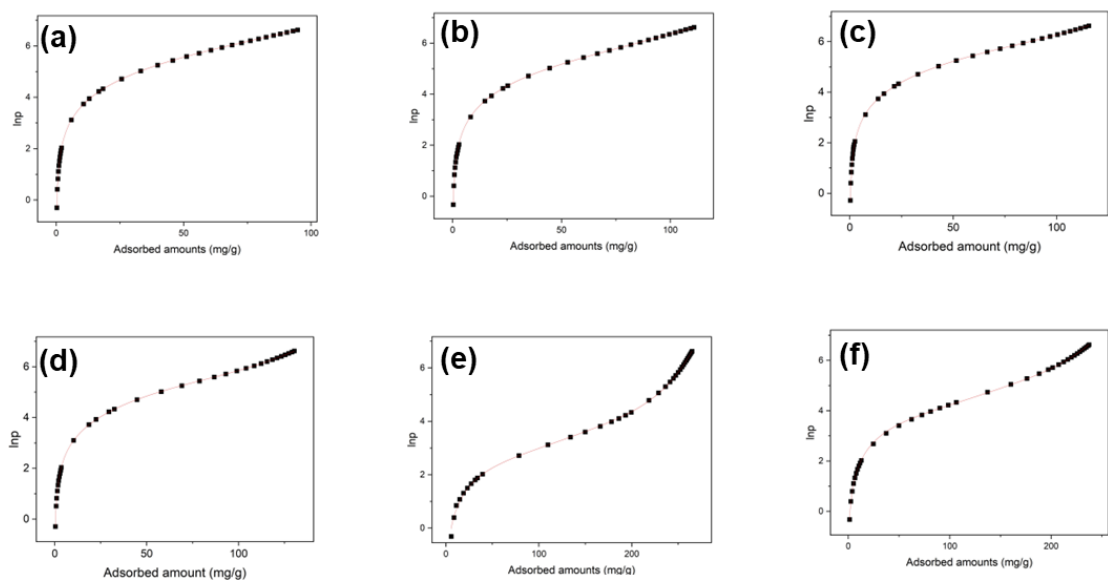
Fig. S11. Virial fitting of MIL-160 for (a)C_2H_4 at 303 K, (b) C_2H_4 at 313 K, (c) C_2H_6 at 303 K, (d) C_2H_6 at 313 K, (e) C_2H_2 at 273 K, and (d) C_2H_2 at 298 K.

Table S2. Virial fitting parameters of MIL-160 for C_2H_4 and C_2H_6.

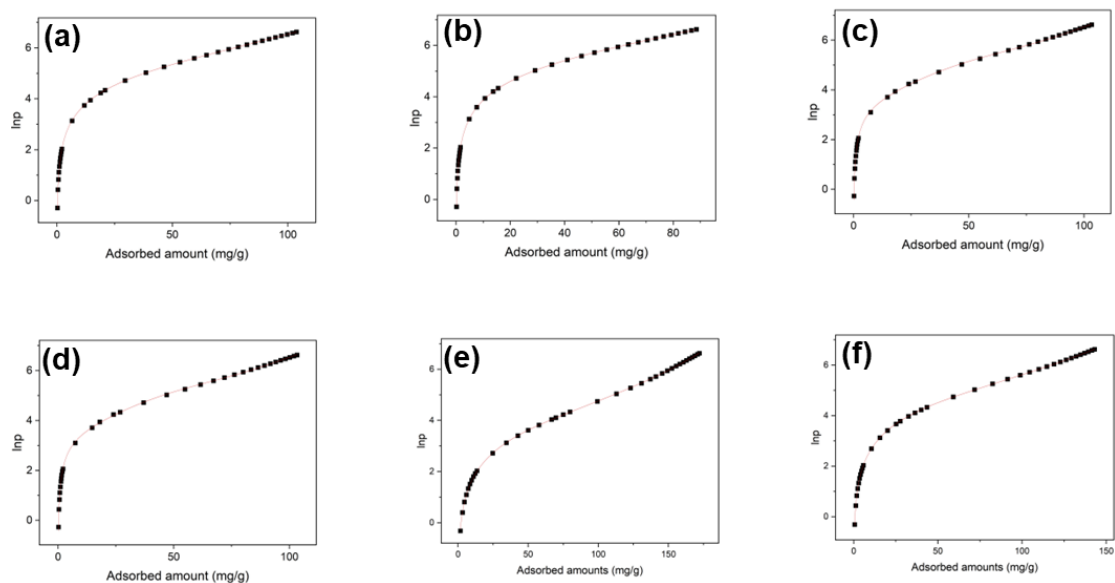| parameters	C_2H_4	C_2H_6	C_2H_2
a0	-3007.94884	-3239.40472	-3927.06549
a1	-22.12306	-7.57022	2.54886
a2	0.21075	0.08016	-0.07981
a3	1.33151E-5	1.18019E-5	-3.06669E-6
a4	-4.33673E-8	-2.71479E-8	5.28225E-9
b0	10.92424	11.47614	12.58462
b1	0.07352	0.0209	5.48841E-4
b2	-4.60806E-4	5.82303E-5	5.03152E-5
R^2	0.99996	0.99998	0.99949

Fig. S12. Virial fitting of CAU-23 for (a)C_2H_4 at 303 K, (b) C_2H_4 at 313 K, (c) C_2H_6 at 303 K, (d) C_2H_6 at 313 K, (e) C_2H_2 at 273 K, and (d) C_2H_2 at 298 K.

Table S3. Virial fitting parameters of MIL-160 for C_2H_4 and C_2H_6.

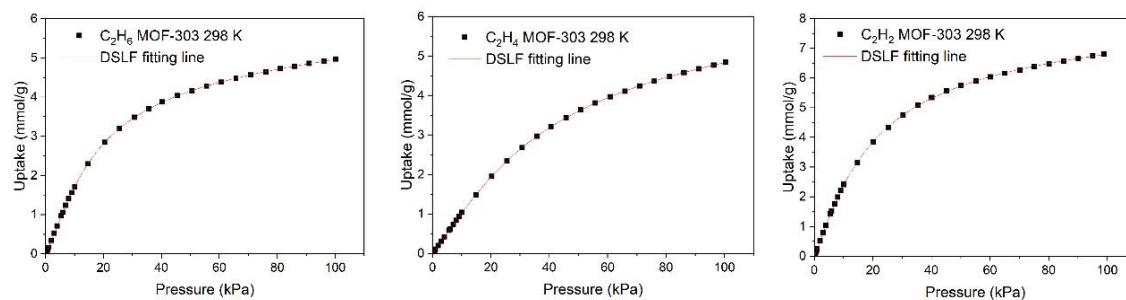| parameters	C_2H_4	C_2H_6	C_2H_2
a0	-2530.67146	-2770.81369	-3256.33055
a1	-24.66003	-9.49445	11.14488
a2	0.20362	0.60694	-0.1147
a3	9.1323E-6	1.12071E-4	-3.9962E-6
a4	-3.40941E-8	-3.43926E-7	8.21577E-9
b0	9.6248	10.29368	11.14173
b1	0.07992	-0.02427	-0.02381
b2	-4.97426E-4	4.52963E-4	1.58449E-4
R^2	0.99999	0.99996	0.99995

S5. IAST selectivity

Fig. S13. DSLF fitting of MOF-303 for C_2H_6, C_2H_4, and C_2H_2 at 298K.

Table S4. DSLF fitting parameters of MOF-303 for C_2H_4, C_2H_6, and C_2H_2 at 298K.

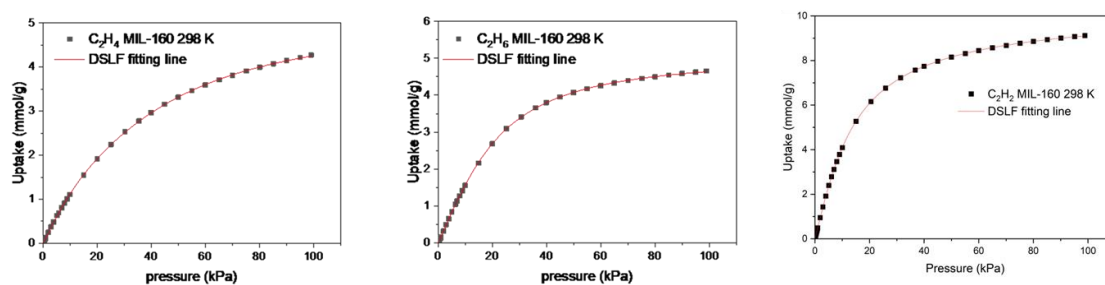| Gas	q1	b1	c	q2	b2	t	R^2
C_2H_4	0.61583	8.15328E-4	2.25816	6.64242	0.01589	1.0248	1
C_2H_6	3.99527	0.02401	1.35758	5.37560	0.01243	0.69499	0.99998
C_2H_2	6.53713	0.02888	1.21839	75.6728	9.91243E-4	0.56525	0.99999

Fig. S14. DSLF fitting of MIL-160 for C_2H_4, C_2H_6, and C_2H_2 at 298K.

Table S5. DSLF fitting parameters of MIL-160 for C_2H_4, C_2H_6, and C_2H_2 at 298K.

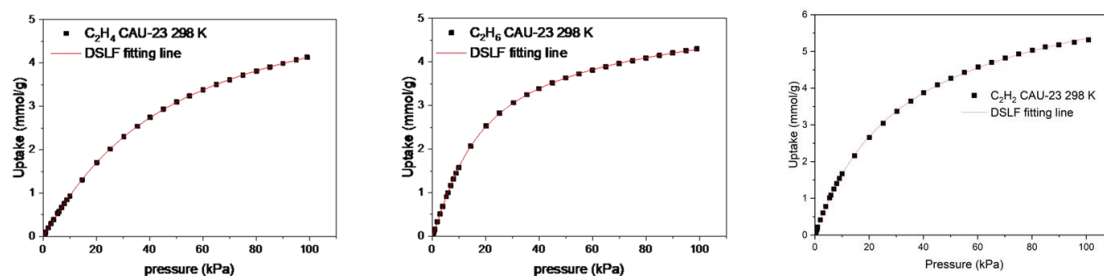| Gas	q1	b1	c	q2	b2	t	R^2
C_2H_4	4.85973	0.02376	1.09809	0.48575	9.1993E-6	2.9375	0.99987
C_2H_6	4.53549	0.01093	1.4965	0.50033	0.27821	1.20044	0.99999
C_2H_2	4.68886	0.02904	1.44335	5.72086	0.0677	0.89864	0.99999

Fig. S15. DSLF fitting of CAU-23 for C_2H_4, C_2H_6, and C_2H_2 at 298K.

Table S6. DSLF fitting parameters of CAU-23 for C_2H_4, C_2H_6, and C_2H_2 at 298K

Gas	q1	b1	c	q2	b2	t	R^2
C_2H_4	4.63101	0.01324	1.18039	4.59371	0.00816	0.6535	0.99999
C_2H_6	3.64785	0.03114	1.27771	4.65721	0.01068	0.68899	0.99998
C_2H_2	3.65842	0.02511	1.1895	5.72684	0.02446	0.70617	0.99992

S6. DFT calculations

DFT calculations for the binding energy of C_2H_2, C_2H_4 and C_2H_6 guest molecules at different levels of coverage in MOF-303, MIL-160 and CAU-23 were performed. The low occupancy structures are given below in Fig. S15 and S16, along with the higher occupancy results in tables S7, S8 and S9. For the case of MOF-303, we were able to bind a maximum of 4 guest molecules per pore. The MIL-160 and CAU-23 MOFs have larger pores and can take up a larger number of molecules in a single pore. With increased occupations, we observe an increase in the total and average binding energy as a result of lateral interactions occurring among guest molecules.
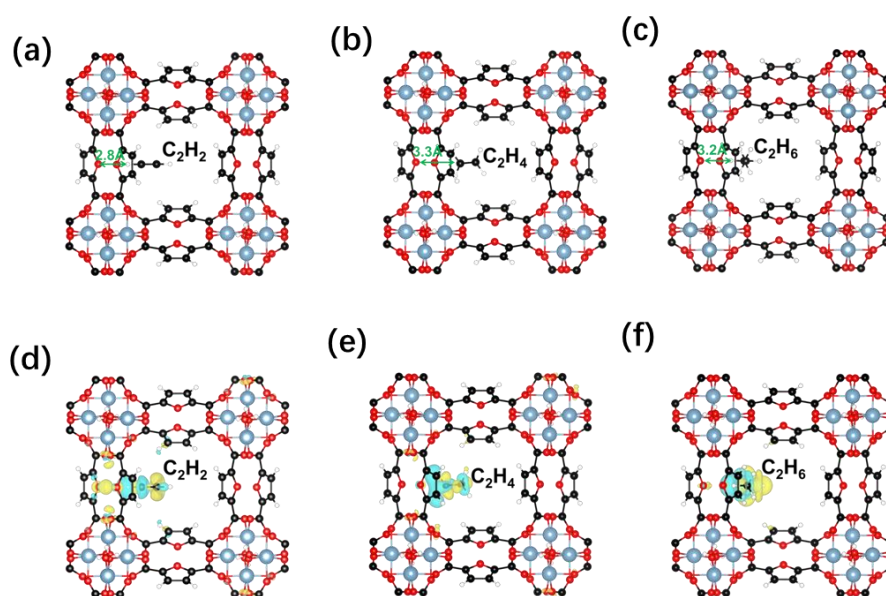

Fig. S16. Primary binding sites in MIL-160 for (a) C_2H_2, (b) C_2H_4, and (c) C_2H_6. Induced charge densities for (d) C_2H_2, (e) C_2H_4, and (f) C_2H_6 at an iso-level of 0.0004 electrons/$Å^3$. The blue areas represent a decrease in charge and yellow areas an increase in charge after binding of the guest molecules.
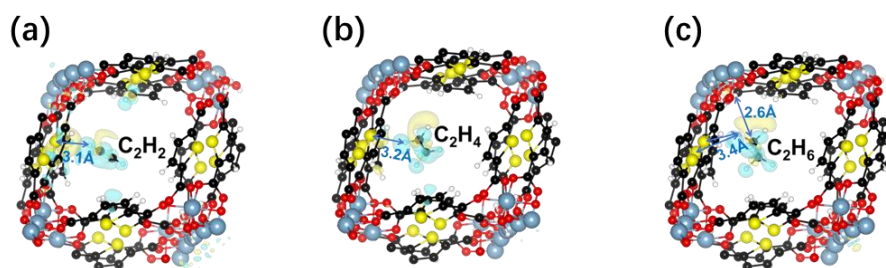
Fig. S17. Primary binding sites in CAU-23 for (a) C_2H_2, (b) C_2H_4, and (c) C_2H_6, showing the induced charge densities at an iso-level of 0.0002 electrons/Å^3. The blue areas represent a decrease in charge and yellow areas an increase in charge after binding of the guest molecules.

Table S7. Average binding energies for increasing concentrations of C_2H_2, C_2H_4 and C_2H_6 in the MOF-303 unit cell.

Guest Molecule	Binding energy per molecule [kJ/mol]
C_2H_2 x 2	52.74
C_2H_2 x 3	53.71
C_2H_2 x 4	63.23
C_2H_4 x 2	42.82
C_2H_4 x 3	46.17
C_2H_4 x 4	47.97
C_2H_6 x 2	57.27
C_2H_6 x 3	57.17
C_2H_6 x 4	57.32

Table S8. Average binding energies for increasing concentrations of C_2H_2, C_2H_4 and C_2H_6 in the MIL-160 unit cell.

Guest Molecule	Binding energy per molecule [kJ/mol]
C_2H_2 x 2	51.55
C_2H_2 x 4	52.29
C_2H_2 x 6	53.80
C_2H_2 x 8	54.68
C_2H_4 x 2	43.56
C_2H_4 x 4	44.87
C_2H_4 x 6	47.53
C_2H_4 x 8	49.60
C_2H_6 x 2	50.96
C_2H_6 x 4	53.16
C_2H_6 x 6	57.95
C_2H_6 x 8	60.11

Table S9. Average binding energies for increasing concentrations of C_2H_2, C_2H_4 and C_2H_6 in the CAU-23 unit cell.

Guest Molecule	Binding energy per molecule [kJ/mol]
C_2H_2 x 2	34.93
C_2H_2 x 4	38.91
C_2H_2 x 6	44.39
C_2H_4 x 2	27.86
C_2H_4 x 4	35.71
C_2H_4 x 6	38.45
C_2H_6 x 2	33.82
C_2H_6 x 4	41.40
C_2H_6 x 6	42.46

S7. Grand canonical Monte Carlo adsorption study

We conducted grand canonical Monte Carlo (GCMC) simulations using the RASPA simulation code[11] to calculate adsorption isotherms for C_2H_4 and C_2H_6 within the three targeted MOFs. Unlike the C_2H_4 and C_2H_6 models used here, there are no sp-hybridized CH interaction groups derived for alkyne modeling. We were unable to get solid agreement using the published C_2H_2 models (which over-adsorbed by up to 50%) that treat the molecule atomically. This led us to focus on C_2H_4 and C_2H_6 for our simulations in the interest of comparability and validity. In these simulations, we considered four different move types: translation, rotation, reinsertion, and swap, with respective probabilities of 0.5, 0.5, 0.5, and 1.0. To capture intermolecular interactions, we set the cutoff distance to 12 Å and employed the Lorentz-Berthelot mixing rules. Periodic boundary conditions were utilized, and the simulation cell lengths were expanded to a minimum of 24 Å in each dimension, thereby preventing any molecule self-interactions.

To ensure equilibration, we performed 10,000 initialization cycles, followed by 100,000 cycles for production runs. Figure S18 illustrates that the equilibrium state was attained quite quickly, hence why few initialization cycles can be used. The pressure was related to the corresponding fugacity using the Peng-Robinson equation of state[12, 13]. During the production cycles, we also recorded different adsorption configurations in order to visualize the density of different binding locations within the pore. The density plots are shown in Figs. S22–S24.

For guest molecules C_2H_6 and C_2H_4 we employed the respective published parameters[14,15]. These models only have Lennard-Jones (LJ) parameters, so the framework was modeled as rigid and neutral, thus, the electrostatic interactions were ignored. The forcefield parameters for the framework's atoms were adapted from the DREIDING[16] forcefield except for the aluminum atoms which were adapted from the UFF[17] forcefield.

Our results using these default parameters qualitatively agreed with the experimental results, however, the adsorption was high overall. Thus, in order to more closely reproduce the experimental results, we adapted the framework parameters by linearly scaling the interaction parameters, employing a similar approach to a previously published method[18]. Since there are only LJ interactions present, we were limited to the energy, or depth of the interaction, and the length parameters. We decided to scale the depth of the interaction and left the LJ length values default. This led to more reasonable agreement with experiment as can be seen in Figs. S19–S21. The modified parameters are in Table S10.

It is essential to recognize that the methodologies employed are classical in nature, thus possessing inherent limitations in capturing the true interaction. Differences between the theoretical and experimental values arise from these approximations.

Despite this, the qualitative agreement helps validate the experimental results, and the density plots help confirm the determined ab initio binding spots, including secondary binding sites enabled by the elevated temperature and higher loadings.
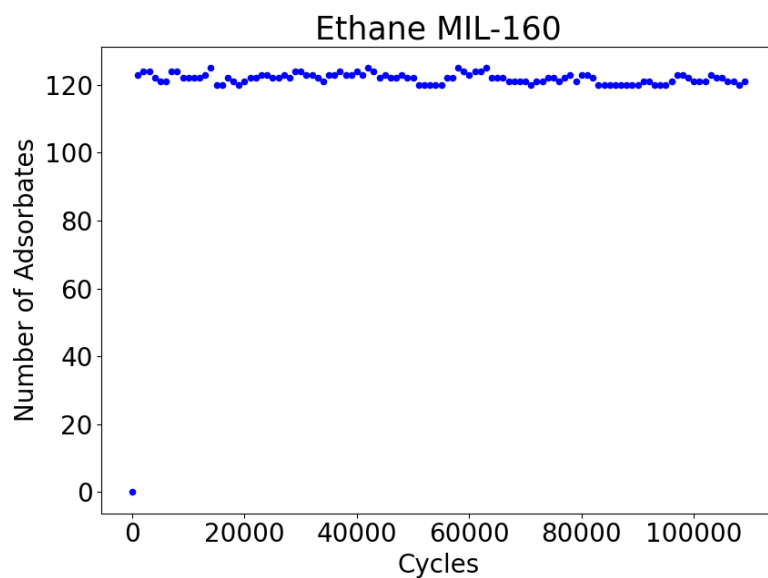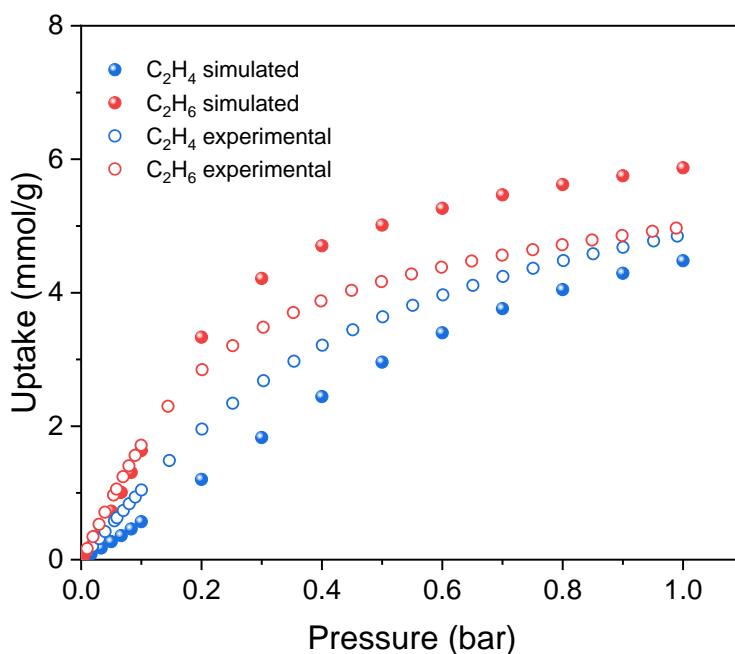

Fig. S18. Equilibration of the system.

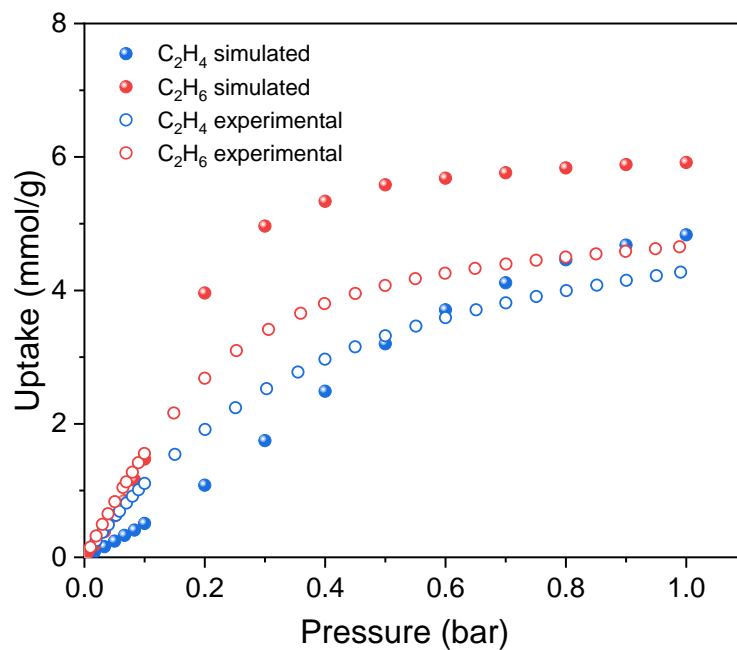Fig. S19. Simulated and experimental adsorption isotherms of MOF-303 for C_2H_4 and C_2H_6 at 298 K.

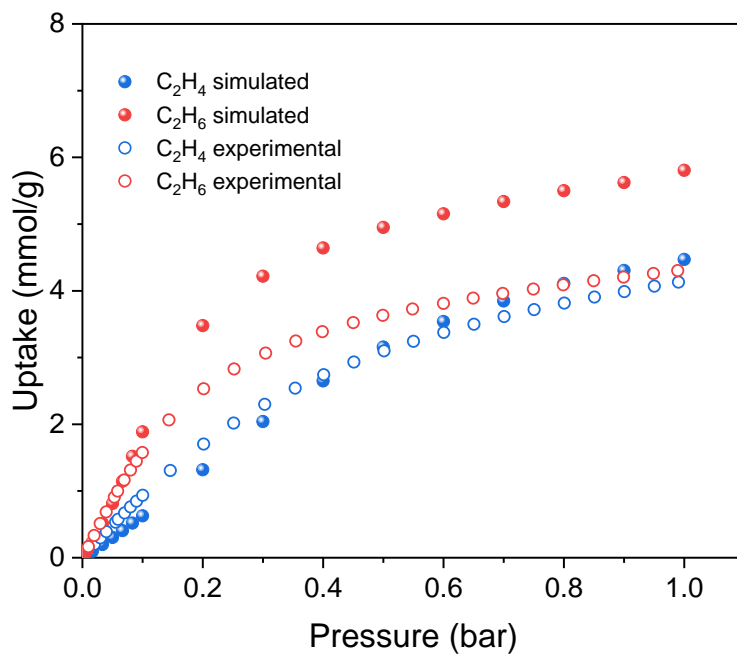Fig. S20. Simulated and experimental adsorption isotherms of MIL-160 for C_2H_4 and C_2H_6 at 298 K.

Fig. S21. Simulated and experimental adsorption isotherms of CAU-23 for C_2H_4 and C_2H_6 at 298 K.

Table S10. Adjusted Lennard-Jones parameters for framework atoms and the force field they originate from.

Atom	ε (K)	σ (Å)	Force Field
O	14.44752	3.40460	Dreiding
C	14.35695	3.89830	Dreiding
H	2.294697	3.19500	Dreiding
N	11.68476	3.66210	Dreiding
S	51.9321	4.03000	Dreiding
Al	76.239	4.49900	UFF

(a)　　　　　　　　(b)　　　　　　　　(c)
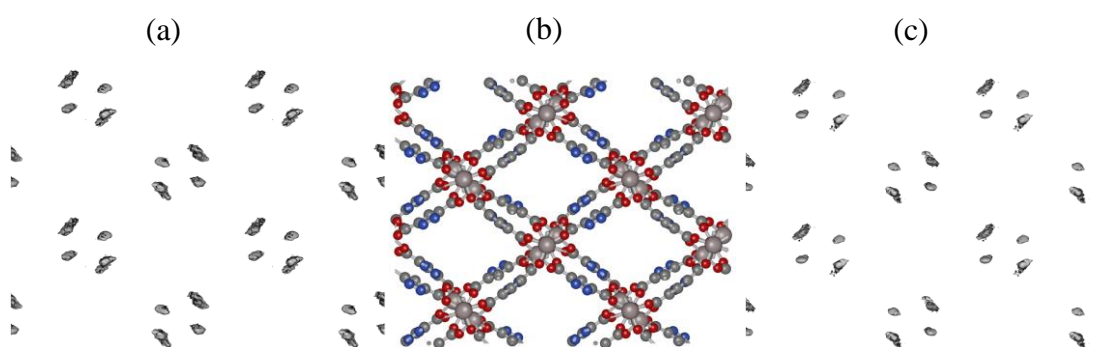
Fig. S22. (a) C_2H_4 binding locations, (b) MOF-303 crystal structure, and (c) C_2H_6 binding locations. In both cases, the binding site by the linker is observed which is in accordance with our DFT results. All molecular probabilities are plotted at a density iso-surface of 0.3.
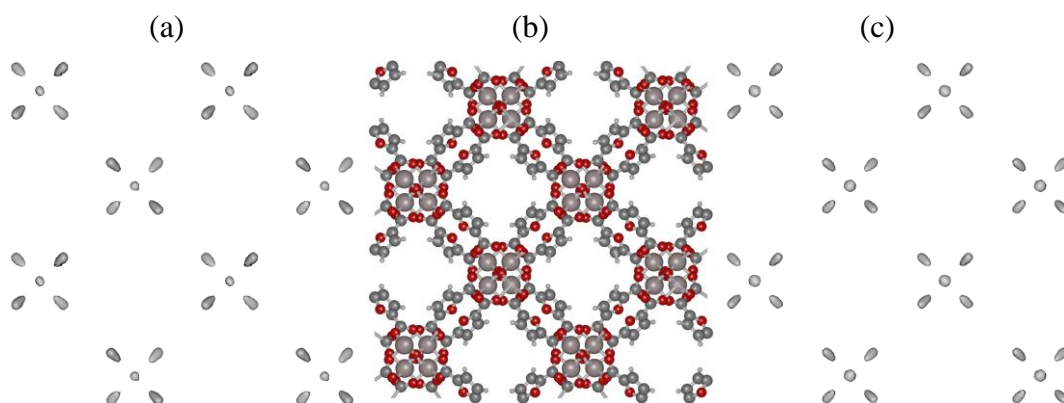
(a)　　　　　　　　(b)　　　　　　　　(c)

Fig. S23. (a) C_2H_4 binding locations, (b) MIL-160 crystal structure, and (c) C_2H_6 binding locations. There is clear agreement with the DFT binding sites, as the binding site by the linker is visable. Additionally, at this temperature, both guest molecule have a secondary binding site present in the center of the pores. All molecular probabilities are plotted at a density iso-surface of 0.3.
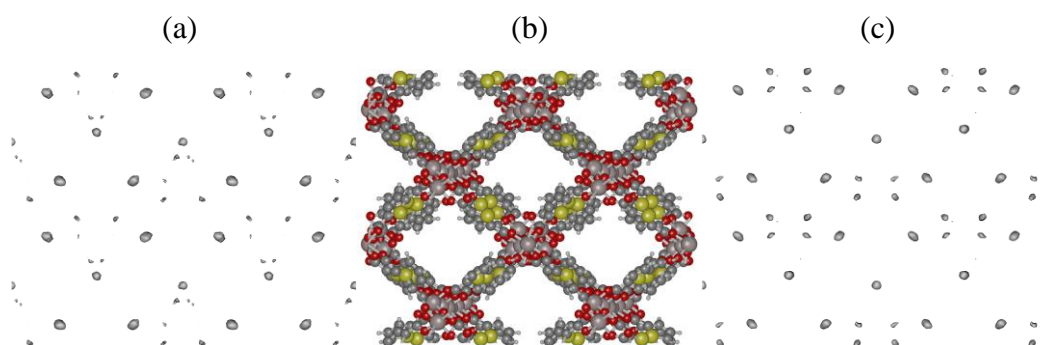
Fig. S24. (a) C_2H_4 binding locations, (b) CAU-23 crystal structure, and (c) C_2H_6 binding locations. In both cases, the binding site by the linker is observed which is in agreement with our DFT results. At this temperature, both guest molecule also exibit a secondary binding site near the O@cluster. All molecular probabilities are plotted at a density iso-surface of 0.3.
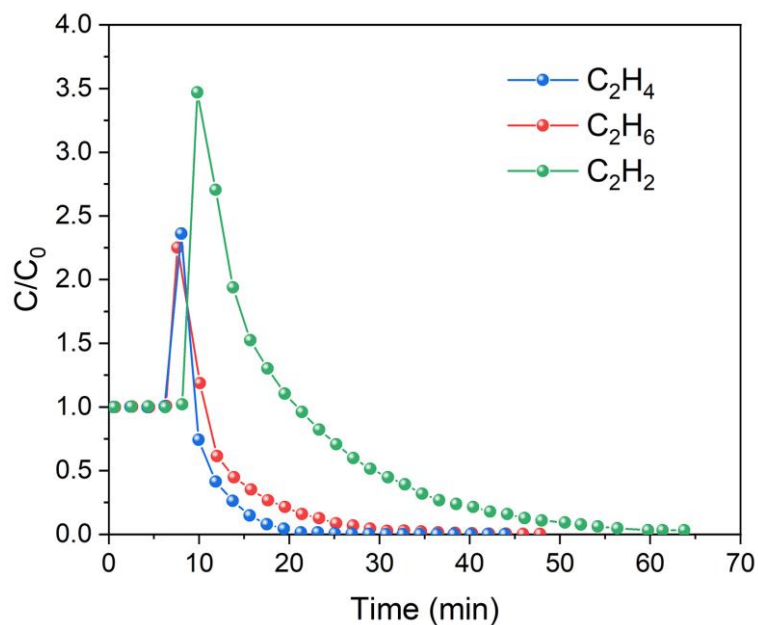
S8. $C_2H_2/C_2H_6/C_2H_4$ desorption curves

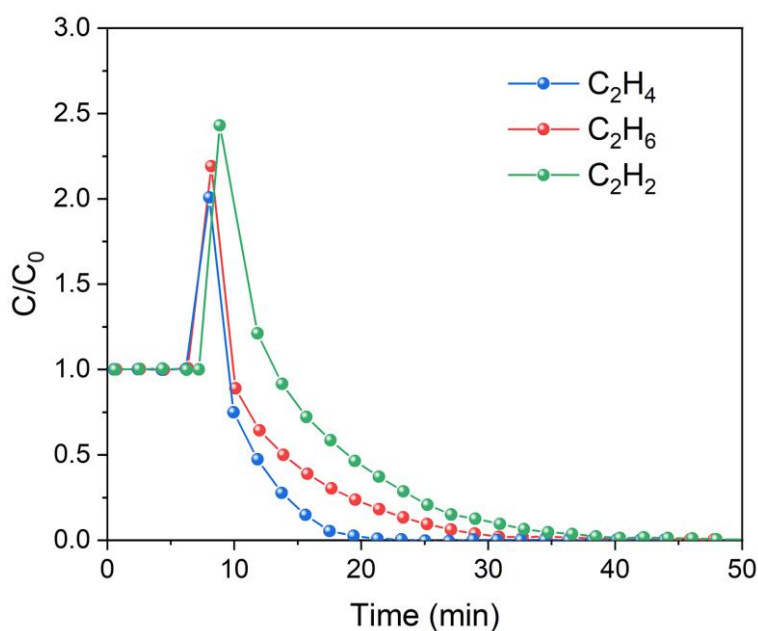Fig. S25. Ternary gases desorption curves for MIL-160 packed column at 323 K under 10 cm^3/min N_2 flow.

Fig. S26. Ternary gases desorption curves for CAU-23 packed column at 323 K under 10 cm^3/min N_2 flow.

S9. C_2H_2/C_2H_6/C_2H_4 adsorption-desorption recyclability and moisture tests
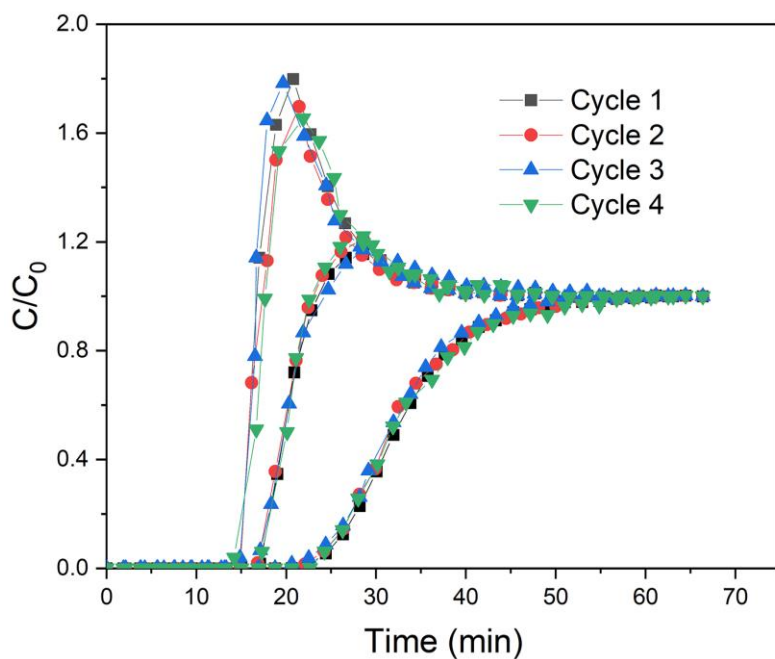

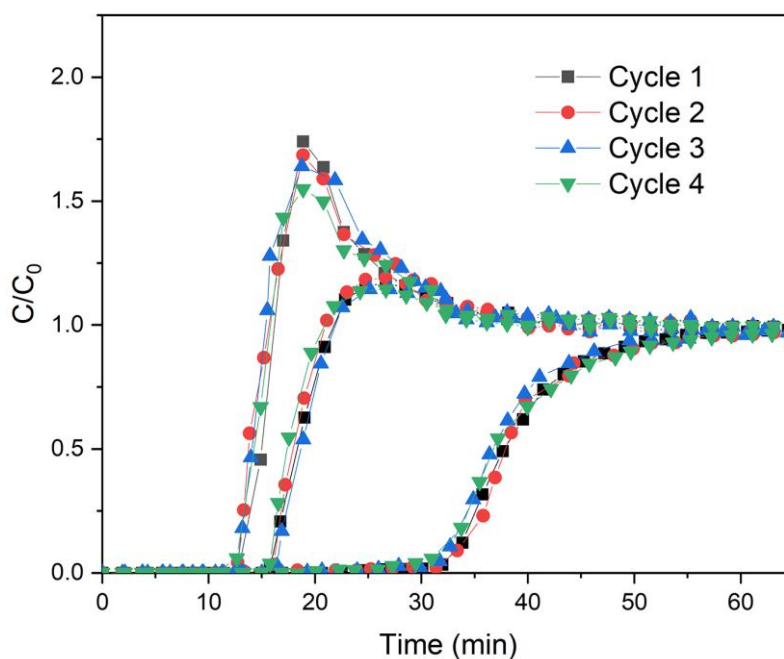Fig. S27. Continuous four times ternary gases breakthrough curves on MOF-303 packed column at 298 K.

Fig. S28. Continuous four times ternary gases breakthrough curves on MIL-160 packed column at 298 K.
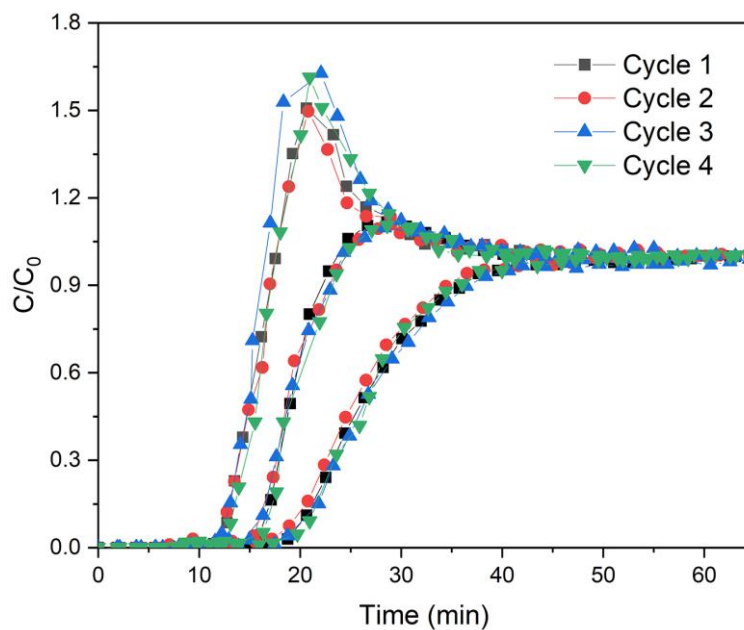
Fig. S29. Continuous four times ternary gases breakthrough curves on MIL-160 packed column at 298 K.
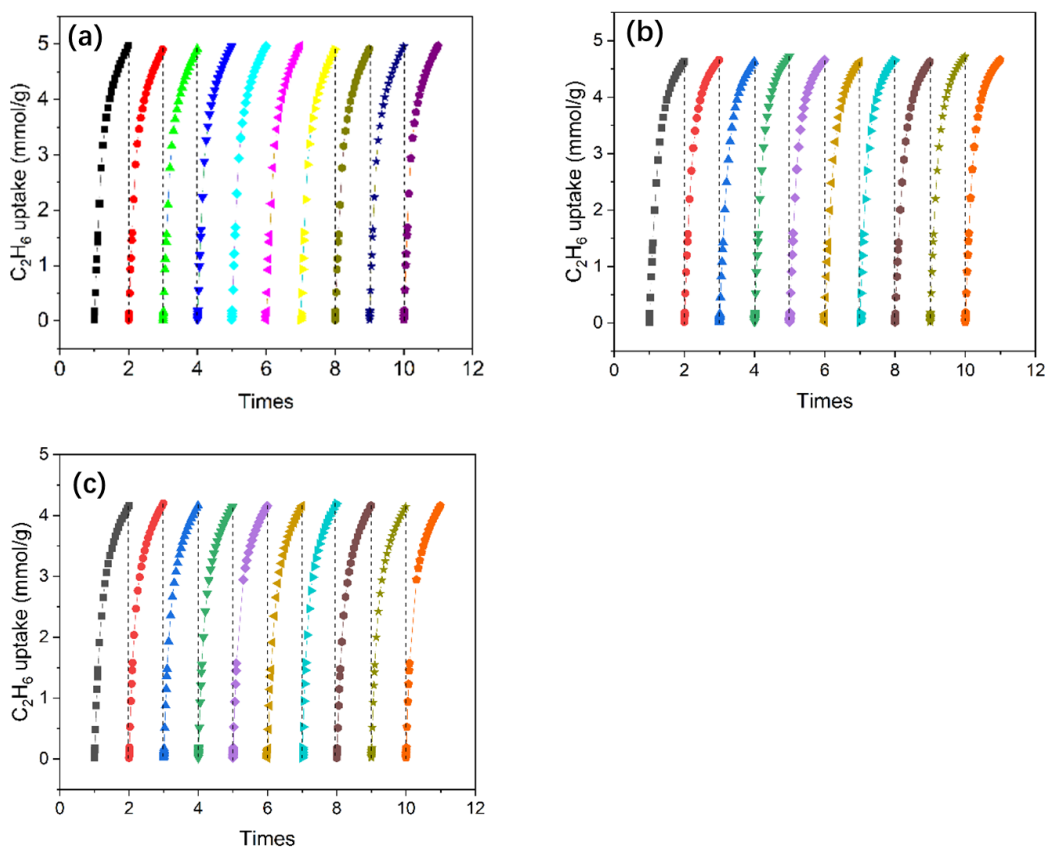

Fig. S30. Ten consecutive C_2H_6 adsorption-desorption cycles on (a) MOF-303, (b) MIL-160, and (c) CAU-23 at 298 K.
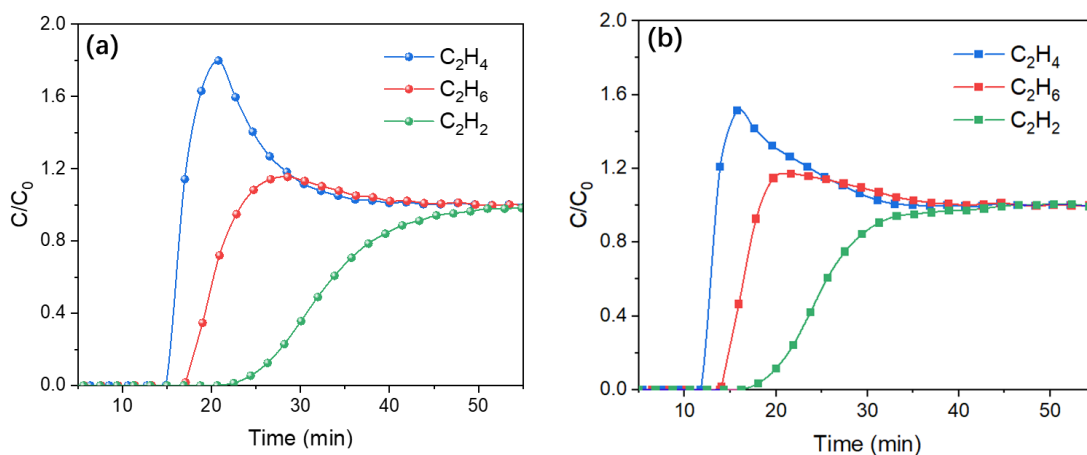
Fig. S31. Breakthrough curves for a ternary gas mixture (C_2H_6/C_2H_4/C_2H_2, 1:1:1, v/v/v) on MOF-303. (a) under dry conditions and (b) with 45% relative humidity at 298 K and 100 kPa.

Table S11. Breakthrough time of C_2H_2, C_2H_4, and C_2H_6 under dry and 45% RH.

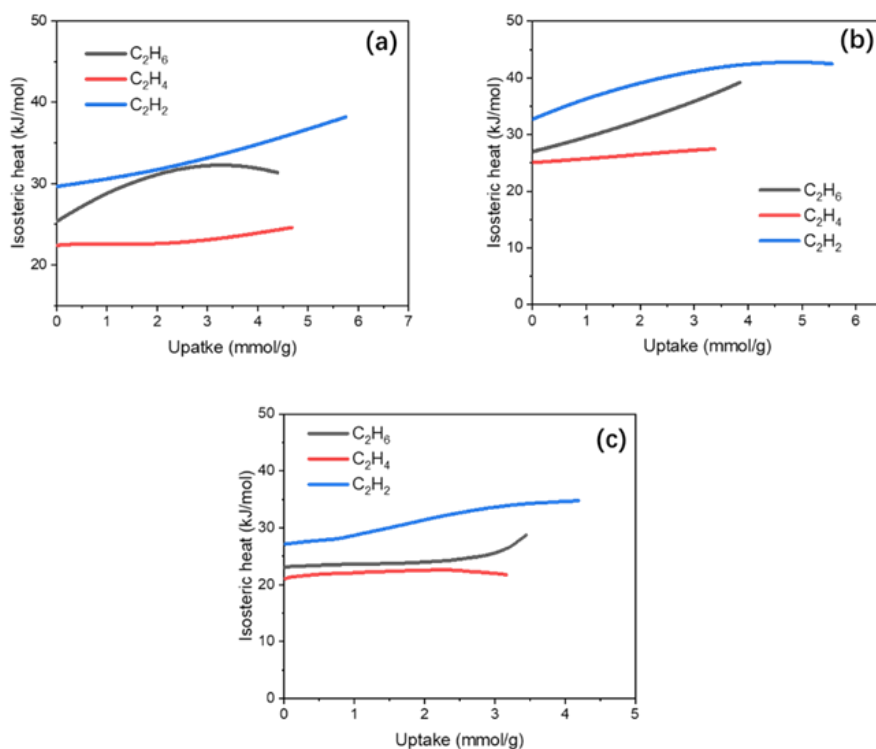| Condition	Breakthrough time (s)		
	C_2H_2	C_2H_4	C_2H_6
Dry	1236	888	1020
45% RH	1026	706	840

Fig. S32. The isosteric heats for C_2H_6, C_2H_4, and C_2H_2 in (a) MOF-303, (b) MIL-160, and (c) CAU-23.

Table S12. The synthetic method of some MOFs and the price of their ligands.
(https://www.aladdin-e.com 2023.06)

MOF	Ligand	Ligand Cost	Synthetic method
Ni(bdc)(ted)$_{0.5}$	Bis(3,5-dicarboxyphenyl)azo	5g / ¥1176.9	DMF/CH$_3$COOH, sealed, 140 °C for 12h
SNNU-40	4'-(3,5-dicarboxyphenyl)-4,2':6',4''-terpyridine'	5g / ¥1586.9	DMA/DMI, sealed, 120 °C for 8 days
CPM-733	2,4,6-tri(4-pyridyl)-1,3,5-triazine	1g / ¥2059.9	DMA/DMP, sealed, 120 °C for 1-4 days
MOF-303	3,5-Pyrazoledicarboxylic Acid	100g / ¥632	Water, 100 °C reflux for 12h
MIL-160	2,5-Furandicarboxylic acid	100g / ¥534.9	Water, 100 °C reflux for 12h
CAU-23	2,5-Thiophenedicarboxylic acid	100g / ¥232.9	Water, 100 °C reflux for 12h

References

1. F. Fathieh, M. J. Kalmutzki, E. A. Kapustin, P. J. Waller, J. Yang and O. M. Yaghi, *Science Advances*, 2018, **4**, eaat3198.

2. G. Kresse and J. Furthmüller, *Physical Review B*, 1996, **54**, 11169-11186.

3. G. Kresse and D. Joubert, *Physical Review B*, 1999, **59**, 1758-1775.

4. K. Berland, V. R. Cooper, K. Lee, E. Schröder, T. Thonhauser, P. Hyldgaard and B. I. Lundqvist, *Reports on Progress in Physics*, 2015, **78**, 066501.

5. D. C. Langreth, B. I. Lundqvist, S. D. Chakarova-Käck, V. R. Cooper, M. Dion, P. Hyldgaard, A. Kelkkanen, J. Kleis, L. Kong, S. Li, P. G. Moses, E. Murray, A. Puzder, H. Rydberg, E. Schröder and T. Thonhauser, *Journal of Physics: Condensed Matter*, 2009, **21**, 084203.

6. T. Thonhauser, V. R. Cooper, S. Li, A. Puzder, P. Hyldgaard and D. C. Langreth, *Physical Review B*, 2007, **76**, 125112.

7. A. Myers and J. M. Prausnitz, *AIChE journal*, 1965, **11**, 121-127.

8. Y. Lin, C. Kong, Q. Zhang and L. Chen, *Advanced Energy Materials*, 2017, **7**, 1601296.

9. Y. Ye, Z. Ma, R.-B. Lin, R. Krishna, W. Zhou, Q. Lin, Z. Zhang, S. Xiang and B. Chen, *Journal of the American Chemical Society*, 2019, **141**, 4130-4136.

10. B. Liang, X. Zhang, Y. Xie, R.-B. Lin, R. Krishna, H. Cui, Z. Li, Y. Shi, H. Wu and W. Zhou, *Journal of the American Chemical Society*, 2020, **142**, 17795-17801.

11. D. Dubbeldam, S. Calero, D. E. Ellis and R. Q. Snurr, *Molecular Simulation*, 2016, **42**, 81-101.

12. D. Frenkel and B. Smit, in *Understanding Molecular Simulation (Second Edition)*, eds. D. Frenkel and B. Smit, Academic Press, San Diego, 2002, DOI: https://doi.org/10.1016/B978-012267351-1/50015-8, pp. 321-387.

13. A. Torres-Knoop, S. P. Balaji, T. J. H. Vlugt and D. Dubbeldam, *Journal of chemical theory and computation*, 2014, **10 3**, 942-952.

14. D. Dubbeldam, S. Calero, T. J. H. Vlugt, R. Krishna, T. L. M. Maesen and B. Smit, *The Journal of Physical Chemistry B*, 2004, **108**, 12301-12313.

15. B. Liu, B. Smit, F. Rey, S. Valencia and S. Calero, *The Journal of Physical Chemistry C*, 2008, **112**, 2492-2498.

16. S. L. Mayo, B. D. Olafson and W. A. Goddard, *The Journal of Physical Chemistry*, 1990, **94**, 8897-8909.

17. A. K. Rappe, C. J. Casewit, K. S. Colwell, W. A. Goddard, III and W. M. Skiff, *Journal of the American Chemical Society*, 1992, **114**, 10024-10035.

18. G. Jajko, J. J. Gutiérrez-Sevillano, A. Sławek, M. Szufla, P. Kozyra, D. Matoga, W. Makowski and S. Calero, *Microporous and Mesoporous Materials*, 2022, **330**, 111555.